Thermal effect on the dynamic infiltration of water into single-walled carbon nanotubes

Jianbing Zhao,[1] Ling Liu,[1] Patricia J. Culligan,[1,*,†] and Xi Chen[1,2,3,*,‡]
[1]*School of Engineering and Applied Sciences, Columbia University, New York, New York 10027, USA*
[2]*Department of Earth and Environmental Engineering, Columbia University, New York, New York 10027, USA*
[3]*Department of Civil and Environmental Engineering, , Hanyang University, Seoul, 133–791, Korea*
(Received 10 August 2009; revised manuscript received 3 October 2009; published 15 December 2009)

Thermally induced variation in wetting ability in a confined nanoenvironment, indicated by the change in infiltration pressure as water molecules enter a model single-walled carbon nanotube submerged in aqueous environment, is investigated using molecular dynamics simulations. The temperature-dependent infiltration behavior is impacted in part by the thermally excited radial oscillation of the carbon nanotube, and in part by the variations of fundamental physical properties at the molecular level, including the hydrogen bonding interaction. The thermal effect is also closely coupled with the nanotube size effect and loading rate effect. Manipulation of the thermally responsive infiltration properties could facilitate the development of a next-generation thermal energy converter based on nanoporous materials.

DOI: 10.1103/PhysRevE.80.061206 PACS number(s): 61.20.Ja, 61.48.De, 62.10.+s, 65.20.Jk

I. INTRODUCTION

Due to its superlative mechanical, thermal, and electrical properties, the single-walled carbon nanotube (SWCNT) is regarded as an ideal candidate for a wide range of applications [1,2], as well as a test bed for fundamental science [3–5]. The large specific area possessed by SWCNT makes it attractive in various nanofluidic applications, including molecular sensors [4], nanopipettes [6], hydrogen storage [7], fluid filtration devices [8], targeted drug delivery devices [9–11], as well as energy related applications such as energy conversion and dissipation [12–16], in which the wettability of a nanotube in aqueous environments plays an important fundamental role in the infiltration and transport of functional liquids within the tube.

Consisting of a rolled sheet of sp^2-hybridized carbon atoms, the SWCNT is generally believed to be nonwettable to water [17]. This phenomenological hydrophobicity is attributed to the weaker interaction potential energy between the confined water molecules and CNT wall atoms (largely owing to the lack of hydrogen bonding [18]). Under ambient conditions, a CNT immersed in water would prefer to remain empty of water [19], and an external pressure is then required to trigger the infiltration of water molecules; the critical pressure at which the capillary resistance can be overcome so that the water infiltration process starts, is termed the infiltration pressure. The magnitude of the infiltration pressure is an effective indicator of the relative hydrophobicity/wettability of the liquid/nanochannel system.

Over the past two decades, intensive research efforts have addressed the wettability of aqueous solutions to SWCNTs [20–22]. For a water droplet confined inside a pristine SWCNT whose radius is between 12.5 and 37.5 Å, the effective water-CNT phase contact angle was found in the range of 104.8°–136.48° at room temperature [23], indicative of a hydrophobic interface. Note that the effective wettability may be strongly affected by a number of parameters, including the surface treatment [20,21], pore structure [24], applied electrical field [25,26], mechanical loading rate [27,28], and temperature [29,30]. Hence, the manipulation of these different parameters may lead to diverse nanofluidic characteristics. Among such parameters, temperature is perhaps the easiest to control during an experiment or a practical application, and thus the thermal effect on the nanofluid infiltration is the main focus of this study.

The thermal effect on wettability is closely related to the well-known thermocapillary effect. For example, an experiment by Shirtcliffe *et al.* [31] showed that as the temperature of a nanoporous MTEOS sol-gel was increased from 390 to 400 °C, the surface switched from superhydrophobic to superhydrophilic. For pressure-induced infiltration of water into zeolite, it was experimentally reported that the required infiltration pressure is a strong function of temperature [32,33], which indicates temperature induced variation in the wettability of the liquid phase. The possibility for temperature to control wetting ability in nanochannels offers promise for the development of a thermal machine based on nanoporous materials, where the thermocapillary effect is dramatically amplified by the large specific pore surface and, as the temperature cycles, the system can output a large mechanical energy density with volume memory characteristics [34].

Despite the aforementioned experimental efforts and the potential of using temperature to control energy related applications of nanoporous materials, the general mechanisms underpinning thermally related effects of liquid infiltration into hydrophobic nanochannel remain unclear. Such mechanisms can potentially be clarified using atomistic simulations, and in this study, we explore the model system of water molecule infiltration into a SWCNT using nonequilibrium molecular dynamics (NEMD) simulations. The system temperature is varied to determine the thermal effects on pressure-driven infiltration. Since the thermal energy is also affected by the loading rate, the coupling between the loading rate and thermal effects is additionally explored. The fundamental molecular mechanisms uncovered in this paper

*Corresponding author.
†pjc2104@columbia.edu
‡xichen@columbia.edu

may provide important insight for the development and optimization of thermally responsive nanofluidic devices [32,34–36].

II. MODEL AND COMPUTATION METHOD

A. Model and simulation procedure

A pristine, straight and long SWCNT is employed as a model nanochannel. Although a stable SWCNT with diameter larger than 1.5 nm may be difficult to fabricate for experimental purposes, such a model system could enable the discovery of fundamental physical phenomena [37]. Several armchair SWCNTs, with structural diameters D ranging from (10, 10) (D=0.81 nm) to (22, 22) (D=2.69 nm) are simulated at different temperatures to reveal the correlation of infiltration pressure with nanopore size, system temperature, and loading rate. The length L of each model SWCNT is around six times of its structural diameter D. For water molecules confined in a nanotube, a depletion zone is formed close to the tube wall, and an effective diameter of the cylindrical volume occupied by water inside the nanochannels can be approximated as $\tilde{d}=(D+D^L)/2$, where D is the diameter of the solid nanotube and D^L the diameter of the water segment in which 95% of the transported liquid is contained [28]; $\tilde{d}$ is an effective measurement of the accessible volume of SWCNT to water, and will be used in relevant analytical calculations.

It is important to note that as the temperature of the system varies, in addition to the changes of the kinetic energy of liquid molecules, the thermally excited oscillation of the solid nanochannel could make a potential contribution to liquid transport behavior. It has been shown that the oscillation of CNT may be potentially employed to transport molecules through nanochannels [38,39]. However, in most previous theoretical/numerical studies on pressure driven infiltration, the flexibility of the nanochannel (e.g., SWCNT) was ignored. Such flexibility might affect both the intrinsic infiltration and transport characteristics of liquid molecules [40]. Therefore, in this study, the SWCNT is flexible (with only the rigid body motion being constrained) and it may therefore deform/oscillate during the infiltration process.

The computational cell (with dimension of $8D \times 2D \times 2D$, where D is the structural diameter of SWCNT) consists of an initially empty SWCNT immersed in a sufficiently large reservoir of water molecules. The water molecules are allowed to diffuse around the nanotube to mimic the actual applications of SWCNTs such as those in biosensor development [41] and gas/liquid adsorption [42,43]; the arrangement of water molecules in this way is believed to be an important step in computing realistic thermal effects, since the water molecules or structures presented outside of SWCNT could impact both the thermal motion of the carbon nanotube [44] and the movement of liquid molecules inside [45]. Periodic boundary conditions are imposed in the four lateral directions, and the reservoir is longitudinally bounded by two rigid "graphene" planes with dimensions exactly the same as the cross section of the computational cell. One of the graphene planes is movable along the axial direction (like a "piston") so as to adjust the volume of the reservoir and thus the pressure of the water. The longitudinal and lateral dimensions of the simulation cell are properly set to allow water molecules to freely "cover" the outer surface of the "isolated" SWCNT. A magnified view near the entrance of the tube is shown in Fig. 1.

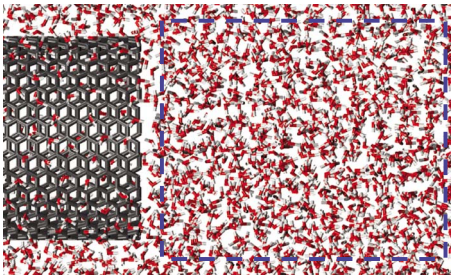

FIG. 1. (Color online) Snapshot of the molecular dynamics (MD) simulation configuration. The armchair (14, 14) single-wall carbon nanotube (SWCNT) is immersed in a reservoir with a sufficient amount of water molecules. The SWCNT can freely vibrate under thermal kinetics energy (with the rigid body motion removed). The water molecules in the reservoir are driven by a rigid plane (which is not shown on the graph), which mimics a piston moving at a constant velocity (loading rate). The region outlined by the dark blue dash line is the sampling zone to numerically calculate the pressure in the reservoir. The system temperature shown is this figure is around 293.5 K, and different temperature levels are adopted in the simulations so as to explore the thermal effect. The tube size and loading rate are also varied and their coupling with the thermal effect is also investigated.

The total number of water molecules, N, is chosen such that the averaged density inside the volume occupied by water is close to that of bulk water, 998.0 kg m^{-3}. The value of N ranges from around 1700 up to 120 000, depending on the dimension of the corresponding SWCNT. Before any load is applied, a relaxation simulation is carried out to minimize the system energy, such that the water/SWCNT system reaches equilibrium at the pore opening to form a stable liquid-vacuum meniscus. Once fully relaxed, a snapshot of the entire liquid-solid system is recorded every 0.5 ps during computation and during the interval between two snapshots, the components of force and stress tensor on each atom are averaged to smoothen the undesirable statistical fluctuation. The simulation typically runs for up to 4.0 ns to obtain enough snapshots for analysis.

The initial pressure in the reservoir is about P =0.1 MPa and the initial temperature is specified at the value of interest (and held fixed throughout the simulation at that given temperature). The pressure in the reservoir is then increased by moving a graphite plane with a prescribed rate to compress the water molecules in the reservoir; the loading rate is varied from 0.05 nm ps^{-1} to 0.2 nm ps^{-1} according to a previous study [13]. The lowest loading rate is numerical verified to produce a minor dynamic effect such that process can be regarded as quasistatic. At any time step, the effective pressure of water, P, is evaluated as follows: within a three-dimensional (3D) cubic sampling region near the entrance of the nanopore (highlighted by the blue dash line in Fig. 1), P is evaluated basing on the intermolecular potential

among water molecules, via the Virial expression $P=N'k_BT/V+\Sigma_i^{N'}\mathbf{r}_i\cdot\mathbf{f}_i/3V$, where N' is the number of water molecules inside the sampling region, k_B the Boltzmann constant, T the system temperature, V the volume of the sample region, and the second term in P accounts for the contribution from the pairwise two-body interaction among the N' water molecules. V is taken to be sufficiently large, inside which the atom/molecule density distribution is nearly isotropic, so that the "local" pressure near the nanotube entrance could be evaluated using the isotropic Virial expression. At each time step, the information of atoms/molecules inside the cubic sampling region quantities (including their positions, velocities, forces on atoms, etc.) is collected to calculate the instantaneous effective pressure. We note that the effective pressure calculated this way not only circumvents the difficulty of computing the anisotropic pressure field inside a nanotube, but also it may be directly compared with experimental values (during a practical experiment the reservoir pressure outside the tube can be measured much more easily than that inside a nanochannel)[1] During the loading process, both the pressure P and variation of volume of the computational cell δV are recorded, from which the infiltration pressure can be determined, as described below.

B. Forcefield

The MD software package LAMMPS [46,47] is adopted to simulate the infiltration process of water molecules into a nominally nonwettable SWCNT. The nonbonding interatomic van der Waals interaction is described by the 12–6 Lennard-Jones empirical force field, $U(r_{ij})=4\varepsilon[(\sigma/r_{ij})^{12}-(\sigma/r_{ij})^6]$, where r_{ij} denotes the distance between atom pairs, and ε and σ are energy and length parameters, respectively. To address the flexibility of the carbon nanotube, the force field of carbon-carbon interaction consists of a Morse potential for stretching, a harmonic cosine potential for bending, a twofold cosine potential for torsion, and a Lennard-Jones (LJ) potential for nonbonding interactions [23,48]. Water molecules are modeled by the extended simple point charge potential (SPC/E) [49]; and to handle the long-range Coulomb interactions, the particle-particle particle-mesh technique (PPPM) is adopted with a root mean square accuracy of 10^{-4} to handle the long range Coulomb interactions among water molecules [50]. The water-carbon interaction is modeled by a single Lennard-Jones term acting between the carbon and the oxygen atom of the water, consistent with the SPC/E water model. The parameters used are $\sigma_{OC}=0.3190$ nm and $\varepsilon_{OC}=0.3135$ kJ mol^{-1}, which correspond to a macroscopic contact angles α of about 105.3° [51,52].

III. RESULTS AND DISCUSSION

A. Infiltration pressure P_{in}

For a representative (14, 14) SWCNT, Fig. 2 presents the MD simulation results where the pressure P is plotted as a function of the volumetric strain of the computational cell $\delta V/V$ (at the loading rate of 0.05 nm ps^{-1}). At any prescribed system temperature, the $P-\delta V/V$ curve shows two distinct stages: the quasilinear compressing stage of water and the empty CNT, and the quasilinear infiltration plateau after the capillary resistance is overcome.[2] The abrupt change of the slope of the $P-\delta V/V$ curve can be used to determine the infiltration pressure, P_{in}. Obviously, P_{in} is a function of the temperature and this point will be elaborated below.

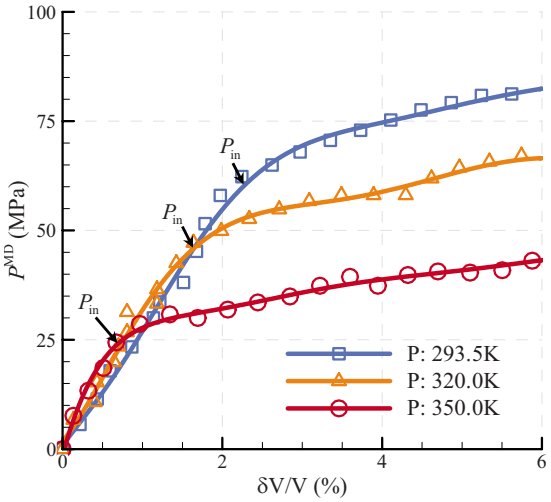

FIG. 2. (Color online) Variations of pressure in the simulation cell as functions of the volumetric strain. The infiltration pressure is defined at the point highlighted by the arrow on the curves, around which the slope of the P-$\delta V/V$ curve changes abruptly. The curves shown here are obtained using a (14, 14) armchair SWCNT as the model nanotube at the temperature of 293.5 K (the upper blue solid line with square symbol), 320.0 K (the middle orange solid line with delta symbol), and 350.0 K (the bottom red solid line with circle symbol), respectively.

In what follows, we first explore the infiltration behavior at the slowest, nearly quasistatic loading rate. The thermal and coupled size effects are presented in Sec. III B and the underlying molecular mechanisms are explained in Sec. III C. The rate effect (and its coupling with thermal effect) is discussed in Sec. III D.

B. Thermal and size effects of infiltration

1. P_{in} versus system temperature T

Figure 2 reveals that, for a given (14, 14) carbon nanotube, the infiltration pressure is reduced as the temperature is increased; and such a general correlation between the infil-

[1]The local pressure near the tube entrance is slightly different than the reaction pressure from water molecules on the moving "piston." Since the former shows less fluctuation during our NEMD simulation (especially at higher loading rates), the local pressure obtained from the Virial expression is employed in the present study.

[2]The infiltration process is reversible upon unloading. Since the carbon nanotubes are geometrically smooth and hydrophobic, the invaded liquid molecules could completely come out the nanotube if the external loading force was taken away and the system was allowed to rest sufficiently. No damage was caused to the physical properties of SWCNT and it was fully restored after a dynamic cycle.

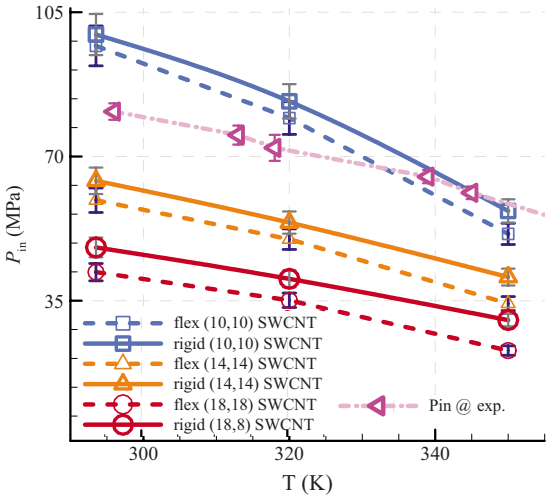

FIG. 3. (Color online) Infiltration pressure variations as a function of environmental temperature. (10, 10) (the upper blue solid and dashed lines with square symbols), (14, 14) (the middle orange solid and dashed lines with delta symbols) and (18, 18) (the bottom red solid and dashed lines with circle symbols) SWCNTs, both rigid and flexible, are studied here to reveal how the temperature and flexibility of carbon nanotube affect the magnitude of P_{in}. The solid color lines are fitted curves on P_{in} from rigid nanotube, and the dashed lines stand for their flexible counterparts. The simulation results from the model (10, 10) SWCNT qualitatively match with the experimental data from Qiao *et al.* [32] (the pink dash-dot line with left gradient symbols), indicating the feasibility of the numerical approach.

tration pressure P_{in} and temperature T is further revealed in Fig. 3 for all tubes being considered. For the (10, 10) SWCNT, the variation trend of P_{in} with T qualitatively match with experimental results reported by Qiao *et al.* [32] using a system consisted of a hydrophobic ZSM-5 zeolite and deionized water. The ZSM-5 zeolite has a pore size of about 1.31 nm, which is on the same order as the diameter of (10, 10) SWCNT (~1.35 nm). Despite the fact that the pore

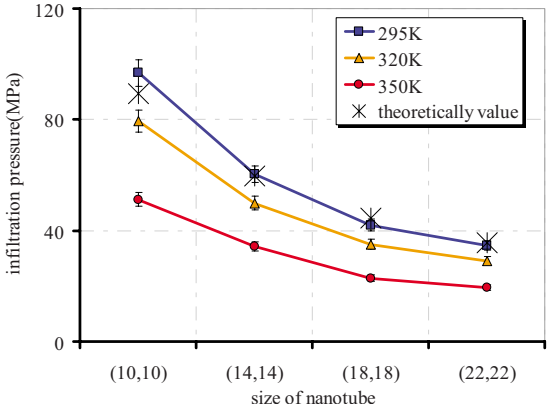

FIG. 4. (Color online) Infiltration pressures as functions of the effective diameters of flexible SWCNT at different temperature levels. The black cross symbols on the graph are theoretical calculations of P_{in}, according to the Young-Laplace equation. The effective surface tension is inversely obtained from the infiltration pressure of the armchair (22, 22) SWCNT at room temperature.

phase and the pore surface structure are different between the zeolite in experiment and the model SWCNT in the current simulation, qualitative agreement of the trend of the infiltration pressure is found.

In order to more clearly uncover the thermal effect, the variation of P_{in} with T of a flexible SWCNT is compared with that of a rigid SWCNT: in both cases, P_{in} reduces nonlinearly with increasing T; and for flexible CNT, P_{in} is lower than that of its rigid counterpart. The difference in P_{in} between a flexible and rigid SWCNT, ΔP_{in}, increases as the tube size gets larger, as well as the temperature gets higher, indicating a coupling between the thermal and size effects. Moreover, for each nanotube, no matter rigid or flexible, the decreasing trend of the P_{in} profile with increasing temperature suggests that at a certain high temperature the pressure barrier for infiltration P_{in} could be reduced to a considerably small value, or even zero, which indicates a temperature-dependent transit from a hydrophobic to a hydrophilic system. Therefore, the fundamental question is: what is the intrinsic mechanism behind the change of wettability? This is explored next.

2. P_{in} versus size of nanotube

As shown in Fig. 4, at a fixed temperature, the infiltration pressure P_{in}, an indicator of the wetting ability, is seen to nonlinearly decrease with increasing effective tube diameter $\tilde{d}$. Note that the infiltration pressure of the largest investigated (22, 22) SWCNT is 35.6 MPa at 293.5 K, and from the classic Young-Laplace equation, $P_{in}=4\gamma_{la}\cos\alpha/\tilde{d}=4\bar{\gamma}/\tilde{d}$ (where γ_{la} is the liquid-gas interface surface tension, α the contact angle between liquid-solid phases, and $\bar{\gamma}$ the equivalent interfacial tension ($\bar{\gamma}=\gamma_{la}\cdot\cos\alpha$) which incorporates the wetting ability of the liquid phase to the solid surface), the value of $\bar{\gamma}$ can be estimated as 19.0 mJ m^{-2}, which matches

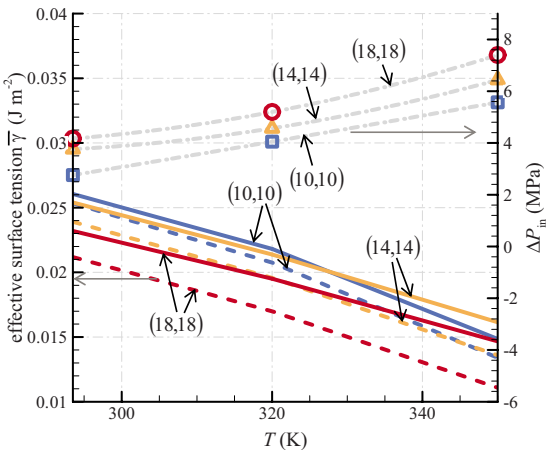

FIG. 5. (Color online) Variations of the effective surface tension $\bar{\gamma}(=\bar{\gamma}_{la}\cdot\cos\alpha$, where γ_{la} is the liquid-air interface surface tension and α the contacting angle between liquid and solid phase) and the infiltration pressure difference ΔP_{in} (between rigid and flexible tubes) as functions of temperature T, for all SWCNTs investigated. The solid lines stand for rigid nanotube and the dashed lines for flexible nanotubes; the gray dash-dot lines indicate the variation of ΔP_{in} with respect to system temperature.

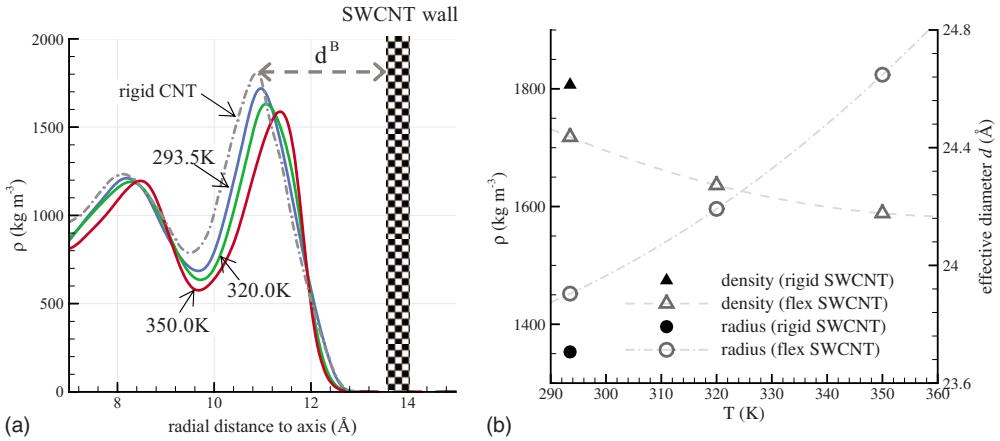

FIG. 6. (Color online) (a) Radial density profiles (RDP) at the entrance of (22, 22) SWCNT for different temperatures. The gray dash-dot line is the result from rigid case at temperature of 293.5 K. d^B on the graph indicates the balanced distance between first solvation shell (FSS) and the nanotube solid wall (the nanotube solid wall position is only illustrated and does not represent the real CNT boundary which is indeed different at different temperatures); (b) distributions of the effective diameter and density value at the FSS in rigid/flexible (22, 22) SWCNTs, with temperature ranging from 293.5 to 350.0 K.

with previous numerical studies of the water-CNT interface [17,23,48]. At the example room temperature of 293.5 K, by using the value of $\bar{\gamma}$ obtained above, a reference infiltration pressure P_{in} can be calculated for each of the other three smaller nanotubes, shown as black cross symbols in Fig. 4. It can be seen that the MD simulations are generally in good agreement with the Young-Laplace equation, in that the MD predicted P_{in} is proportional to the inverse of the effective diameter $\tilde{d}$.

3. Thermal and size effects on interface tension

Based on the value of P_{in} obtained from MD simulations, from the Young-Laplace equation the effective surface tension $\bar{\gamma}$ can be calculated for all nanotubes and at different temperatures, Fig. 5. In general, when the tube size is fixed, $\bar{\gamma}$ decreases at higher temperature; while at a given temperature, the larger nanotube possesses a smaller value of $\bar{\gamma}$. When comparing between rigid and flexible tubes, the flexibility of the nanotube exerts its influence by reducing the effective magnitude of $\bar{\gamma}$; and such a reduction in $\bar{\gamma}$ (with respect to its rigid counterpart) is found to increase as the size of nanotube increases and as the temperature rises. For different tube sizes, e.g., (10, 10) and (18, 18), the slopes of the $\bar{\gamma}-T$ profiles are different, indicating a coupling between thermal and size effects. Details of the tube size effect on the surface tension of confined nanofluids at ambient temperature conditions have been reported in the literature [53]. Here, we focus on the thermal effect and its coupling with the tube size effect.

Note that since $\bar{\gamma}=\gamma_{\text{la}}\cos\alpha$, the size and thermal dependencies of $\bar{\gamma}$ includes that of γ_{la} and contact angle α—the later may be obtained via a statistical study of the shape water molecule front, reported in another work of our group [30].

Also shown in Fig. 5 is the difference in infiltration pressure, ΔP_{in}, between a rigid SWCNT and its flexible counterpart, which is noticed to be a strong function of both the tube size and the environmental temperature. Generally, ΔP_{in} increases as the tube size gets larger and as the temperature gets higher. In conjunction with Fig. 3, the thermal dependency of P_{in}, which is underpinned by the thermally induced variation in wetting ability, arises from changes in the molecular structure of confined water molecules, as analyzed below.

C. Discussion: Molecular mechanism of thermal effect

1. Variation of effective tube radius due to thermal oscillation

Figures 6(a) and 6(b) shows the radial density profiles (RDP) obtained in a (22, 22) SWCNT, sampled near the entrance of the tube and during the infiltration process; the RDP for the flexible tube at different temperatures are compared with that obtained in the rigid nanotube, with a special focus on the position of the first solvation shell (FSS). The RDP in the rigid carbon nanotube, especially the position of the FSS, is found to be almost invariant with temperature, thus its profile obtained at room temperature (293.5 K) is listed for reference [the gray dashdot line in Fig. 6(a)].

In Fig. 6(a), comparing with the rigid counterpart, the position of the FSS in the flexible nanotube is found to move away from the nanotube axis,[3] and its density ρ^{FSS} correspondingly decreases, which is also shown in Fig. 6(b). This observation is straightforward because the flexibility of SWCNT provides the invaded liquid phase more freedom for volumetric expansion in radial direction. Since the RDP is currently measured from the axis of nanotube, the effective diameter $\tilde{d}$ could be estimated with respect to the FSS position and its equilibrium distance d^B to the nanotube wall. In Fig. 6(b), as expected, at the same room temperature, the

[3]On the other hand, if the RDP is measured and normalized using the distance from the SWCNT wall, the position of the first solvation shell would overlap, with the magnitude of density there remains a function of temperature.

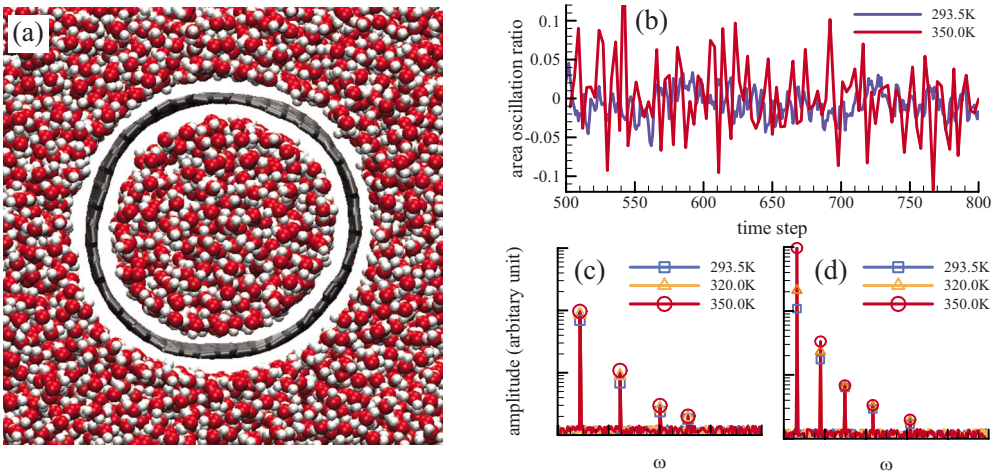

FIG. 7. (Color online) Graphic illustration of the thermal oscillation of the end area of the CNT. (a) The contour of the CNT end has been obviously distorted by the coupled thermal motion with surrounding water molecules; (b) the time histories of the cross-section area (at tube entrance) oscillation within a certain sampling window for the (22, 22) SWCNT at the temperature of 293.5 and 350.0 K, respectively; (c) spectrum distribution for the (14, 14) SWCNT end area's thermal oscillation, obtained from fast Fourier transform (FFT) analysis; (d) spectrum analysis for the (22, 22) SWCNT end area's thermal oscillation.

flexible nanotube's effective diameter $\tilde{d}$ is found to be larger than that of the rigid counterpart, which could be a factor contribution to the reduced P_{in} of flexible SWCNT in Fig. 3 (comparing with the rigid counterpart), according to the Young-Laplace equation. Another feature observed on Fig. 6(b) is that the effective diameter $\tilde{d}$ in the model (22, 22) flexible SWCNT is found to be a strong function of the ambient temperature T with a trend of increasing diameter with elevated temperature, and this dependency is qualitatively consistent with the increasing trend of ΔP_{in} in Fig. 5.[4]

Particularly, the outward movement of the FSS is believed to closely relate with the thermal oscillation of the wall of SWCNT. Presented on Fig. 7(a) is a snapshot of the transient deformation of the (22, 22) SWCNT surrounded by water molecules, at the moment when infiltration starts. Fast Fourier transform (FFT) analyses are performed for the histories of the area oscillation at the inlet of the CNT at 293.5 and 350.0 K, respectively [Fig. 7(b)]. The spectrum distributions of both (14, 14) and (22, 22) SWCNTs are listed: the basic mode frequencies are found to qualitatively match with the previously reported breath frequency of CNTs immersed in water [22,44]. The majority of the thermal oscillating energy is concentrated on the basic mode. For the smaller (14, 14) SWCNT, a relatively small variation is noticed in the amplitude of each oscillating mode as the temperature is increased, Fig. 7(c); however, for the larger (22, 22) SWCNT, the thermal oscillating energy of the basic mode demonstrates strongly thermal dependency, Fig. 7(d). The intensified oscillation helps to agitate the random thermal motion of water molecules that then increases the effective diameter $\tilde{d}$ of FSS.

However, for a flexible (22, 22) SWCNT, the increase in the effective diameters $\tilde{d}$ from 1.253nm at $T=293.5$ K up to 1.293nm at $T=350.0$ K (according to Fig. 6) only accounts for $\sim 4\%$ of the drop in the magnitude of P_{in}, (using the Young-Laplace equation); such a reduction in P_{in} does not match with the prominent decreasing trend observed in Figs. 3 and 4. Thus, other than the geometrical factor, the change of the basic physical properties of water molecules with temperature may be a more important factor reflecting the thermal effect.

2. *Thermal variation of hydrogen bonding*

In essence, when T is higher, the water molecules possess more kinetic energy thus require less external energy to overcome the energy barrier presented at the entrance of the nanotube. Examining the variation of P_{in} with T in a rigid nanotube (Fig. 3), the magnitude of P_{in} drops by almost 40% when T increases from 293.5 to 350 K. At the atomistic level, the hydrogen bond (H-Bond) among water molecules is well known to govern many essential physical properties of water, such as density, surface tension, boiling point, and viscosity. A H-Bond is supposed to occur between two water molecules if (a) the O-O distance is less than 3.5 Å, and (b) the O-H…O angle is less than 30° [54]. Using a TIP4P water model, the number of hydrogen bonds per water molecule, n_{HB}, at room temperature was found to be about 3.59 for bulk water [55], which is close to the value recovered in our MD simulations. In Fig. 8, the time averaged H-Bond number density (per water molecule) at the entrance of a (22, 22) SWCNT is presented for different temperatures, and for both

[4]To further generalize the current MD simulations, an interesting scenario would be the situation when there were no water molecules surrounding the carbon nanotubes, which is the case of immersing a closely compacted cluster of strongly hydrophobic carbon nanotubes in an aqueous environment, and is different from the currently adopted MD model. Water molecules absorbed on the inner or external surface of carbon nanotube are known to alter its radial oscillation mode [44]. With no water molecules presenting externally, the CNT is allowed more freedom in radial oscillation with a decreased basic frequency in radial oscillation [44]; a greater radial thermal oscillation amplitude would have the effect of further lowering the infiltration pressure.

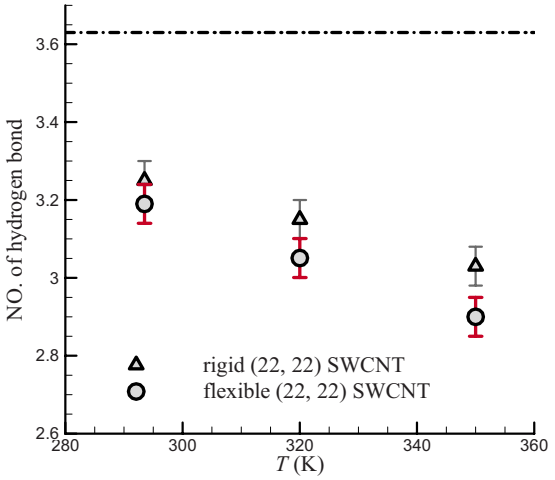

FIG. 8. (Color online) Time averaged hydrogen bond (H-Bond) number of water molecules as they infiltrate into a (22, 22) SWCNT. The number of H-Bond is averaged over snapshots of the MD results obtained at a frequency of 50ps. The dash-dot line indicates the time averaged H-Bond number for bulk water molecules at room temperature.

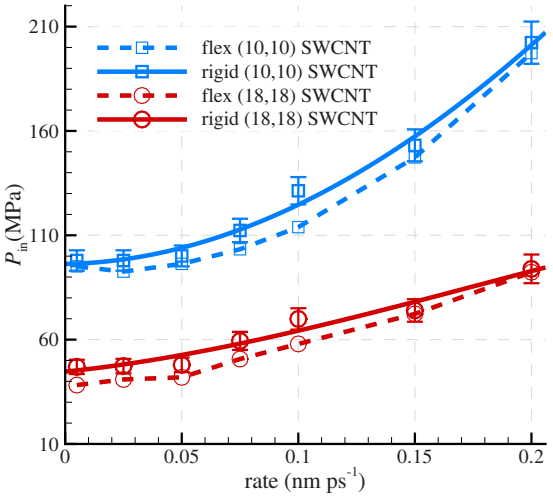

FIG. 9. (Color online) Variations of the "apparent" P_{in} with loading rate $\bar{v}$, obtained at room temperature 293.5 K. Results from (10, 10) (the upper blue solid and dashed lines with square symbols) and (18, 18) (the lower red solid and dashed lines with circle symbols) SWCNTs are compared. The solid lines stand for results obtained by rigid nanotube models; while the dashed lines with symbols are their flexible counterparts.

rigid and flexible cases. Due to the nanoscale confinement, the water molecule normally needs to lose part of its hydrogen bond as it enters the nanotube, leading to a generally smaller value of n_{HB}. For the rigid tube, n_{HB} is 3.26 at $T=293.5$ K and drops to 3.03 at $T=350.0$ K. Seemingly marginal, such a decrease in hydrogen bonding could actually lead to great variation in wetting ability, in terms of the magnitude of surface tension [56], and that can be the dominant factor which explains the dramatically descending trend of P_{in} with increasing temperature, as observed in Fig. 4.

Additionally, in a flexible SWCNT, the thermal excited oscillation of nanotube wall may further destabilize the H-Bond among water molecules [57] and facilitate the mobility of molecules [38,39]. Figure 8 shows that when the flexibility of the nanotube is being considered, n_{HB} decreases to about 3.19 at $T=293.5$ K and the reduction of n_{HB} is more prominent at a higher temperature T ($n_{HB}=2.91$ at $T=350.0$ K). Considering the stronger amplitude at higher temperatures (Figs. 7(c) and 7(d)), the thermally intensified radial oscillation of CNT is believed to enhance the thermal motion of water molecules, thus weakening their hydrogen binding interaction. Moreover, since the radial oscillating amplitude in a smaller SWCNT is smaller compared to a larger tube, it is speculated that the reduction in n_{HB} in a smaller nanotube could be minor. This is consistent with the relatively small ΔP_{in} in the (10, 10) SWCNT (the gray dash-dot line with square symbol), as shown in Fig. 5, illustrating the coupling between tube size and thermal effects.

D. Loading rate effect of infiltration

The above comparisons reveal a strong thermally induced dependency of the quasistatic infiltration process. However, in practical applications such as absorbing impact energy using nanoporous energy absorption system (NEAS), the liquid molecules could infiltrate and transport inside the nanotube at a high rate [17,58], during which process part of the mechanical work may be continuously dissipated via "friction" between the solid and infiltrated liquid molecules, which could increase the system's temperature. The shear stress of dissipation is a strong function of loading rate [59], and thus the loading effect is coupled with the thermal effect (energy). In this section, we assume that the temperature of the system maintains at a series of desired constant values during the infiltration process, and explore the rate effect on the infiltration pressure.[5]

As the loading rate (of the piston) $\bar{v}$ is increased, Fig. 9 shows the variations of the apparently measured P_{in} at 293.5K, for (10, 10) and (18, 18) flexible/rigid SWCNTs. It is found that the measured P_{in} monotonously increases as the loading rate gets faster, and such a trend is more apparent for the smaller sized nanotube, showing the coupling between size and rate effects [13,28]. It is well known that a pressure surge ΔP occurs when a liquid flow is suddenly decelerated; this phenomenon is termed water hammer in hydraulics and its magnitude can be approximately evaluated as $\Delta P \propto \rho c \bar{v}$, where ρ is the density of the liquid and c the sound speed in the liquid at the given temperature [60]. Upon dynamic loading on the piston, the liquid molecules inside the reservoir experience a similar fast deceleration, which causes a sudden increase in the local pressure (pressure surge) near the nanotube entrance; and the liquid-vacuum/air meniscus acts as an elastic membrane buffer which greatly smoothes the sharp pressure pulse. Moreover, the compressibility of the liquid

[5]The system temperature was artificially fixed constant due to the fact that the initial infiltration process could be approximated as a quasielastic process with trivial joule heat generated. Such an approach has been experimentally verified feasible since no substantial temperature increment had been observed before infiltration occurring.

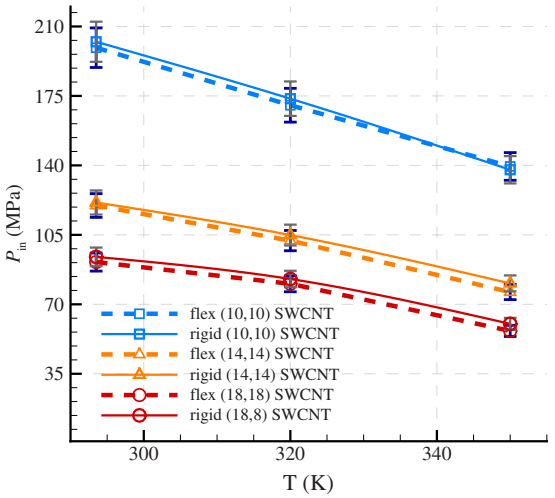

FIG. 10. (Color online) Comparison of infiltration pressure for both rigid and flexible SWCNTs as functions of temperature. The loading rate is 0.2 nm ps^{-1} and (10, 10) (the upper blue solid and dashed lines with square symbols), (14, 14) (the middle orange solid and dashed lines with delta symbols) and (18, 18) (the bottom red solid and dashed lines with circle symbols) SWCNTs were used as the model nanotubes.

phase and the reduction of wetting diameter accessible to the liquid phase due to the geometrical deformation of the nanopore under the high confining pressure will both contribute to a higher sound speed c in the liquid phase [60], which then directly results in a larger pressure increment.[6] Consequently, a higher loading rate leads to a higher "apparent" P_{in}—in essence, the higher loading rate results in stronger compressibility of liquid phase and geometrical deformation of the nanopore, which, in turn, contributes to a stronger pressure surge for an increased loading rate. Thus, a positive feedback can be concluded to occur between the apparent infiltration pressure and loading rate (Fig. 9).

On Fig. 9, it is also noticed that at a smaller loading rate there is a difference between the apparent infiltration pressures of rigid and flexible SWCNTs; however, the difference ΔP_{in} almost vanishes as the loading rate $\bar{v}$ becomes faster. That is, the faster loading rate seems to be able to constrain the thermal oscillation and deformation of the CNT. This suppressed thermal effect is more obvious on Fig. 10, where the "apparent" P_{in} for flexible SWCNT almost overlaps with that of its rigid counterpart at the higher loading rate of 0.2 nm ps^{-1}, for all tubes examined. Comparing Figs. 3 and 10, one can identify the coupling between rate and thermal effects: for all CNTs investigated, at a low loading rate, the thermal energy affects the infiltration behavior through both the thermally changed physical property of water and the thermally enhanced radial oscillation of the flexible nanotube (Fig. 3). Whereas at a faster loading rate, before the meniscus undergoes further change, the reservoir pressure could sufficiently suppress the thermally induced oscillation of the CNT, making the flexible CNT rigidlike, as shown in Fig. 10. The major contribution to the thermal effect is the variation in water physical properties at higher temperature.

[6]It should be noted that the sudden increase in local pressure (pressure surge) at the inlet of nanotube does not lead to a change in the wetting ability of the solid phase to the liquid phase. This pressure surge is triggered by variations in physical properties of the liquid phase and the geometrical configuration of solid phase, which reflects the transient reaction of the solid-liquid system when exposed to dynamic external loading.

TABLE I. (Color online) Contribution of each system factor to variation of wetting ability (change of infiltration pressure P_{in}). The horizontal and vertical axes point in the direction of increasing system variables; the sign of projection of the inclined arrows on the axes indicates the correlation between infiltration pressure P_{in} and the corresponding system variable: positive means an elevated P_{in} with an increasing system variable, and negative means the opposite. For example, increasing either the nanotube size or the environmental temperature would individually decrease the infiltration pressure, so that the arrow in element (1, 2) or (2, 1) of the above matrix points to lower left, with projections on both axes are negative. In general, a larger P_{in} implies better energy absorption performance in the nanoporous energy absorption system (NEAS) [12], which is adjustable via the pore size, loading rate, and temperature as discovered in this paper.

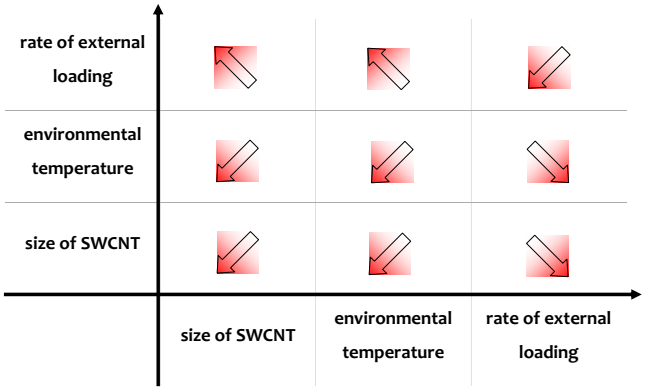

IV. CONCLUDING REMARKS

Using NEMD simulations, it is found that the elevated thermal energy of the water-CNT system decreases the critical pressure barrier and makes it easier for water molecules to infiltrate into a SWCNT, that is, the wetting ability is effectively increased. Detailed molecular structural analysis reveals such an enhancement in wetting ability is underpinned by the thermal effect on key system variables, including enlarging the accessible entry area of the nanotube (via the thermal oscillation of SWCNT shell wall), and weakening the intermolecular bonding interaction (H-Bond) by the enhanced thermal motion of water molecules at higher temperature, with the later factor more dominant to effectively reduce the surface tension of the confined water phase at higher temperature. The effect of thermally induced radial oscillation of SWCNT is closely coupled with the tube size and loading rate. At much lower loading rates (quasistatic status), the drop in P_{in} increases for a bigger tube (fixed temperature) and a higher temperature (fixed tube size); while at a much faster loading rate, the tube's flexibility is

effectively suppressed by the quickly elevated confining pressure and the infiltration behavior of the carbon nanotube becomes more rigidlike. Moreover, in a smaller SWCNT, the magnitude of P_{in} is higher and its trend with loading rate $\bar{v}$ is more nonlinear. The individual and coupled effects of these factors (thermal, size, and rate effects) on the variation of infiltration pressure are summarized in Table I.

The current numerical study thus provides valuable information for choosing proper liquid and solid phases (as well as working temperature) for certain applications, for example, enhancing the energy absorption performance of the NEAS through the guidelines in Table I. Due to the complexity of the real infiltration process, other effects, such as the surface chemical properties, and the geometry/surface roughness of the nanopore, could also strongly impact the infiltration process and will be studied in future. The study also shed some light on the development of a phenomenological model. For example, by taking into account the coupled thermal dependence, size dependence, and rate dependence of the effective contact angle and surface tension, the infiltration pressure could be well predicted by the phenomenological model that is modified from the conventional fluids theory [30].

The thermally induced dependency of infiltration behaviors arouses the necessity of balanced design of nanofluidic devices to either prompt or depress the thermal oscillation of nanochannels. In the research of next-generation thermoelectric converter using nanochannels, e.g., carbon or ZnO nanotubes with diameters smaller than 2 nm [61], the thermally induced oscillation of a nanotube could help to reduce the infiltration pressure barrier to selectively convey liquid molecules/ions through the nanochannels, so as to more effectively utilize the subtle thermal energy difference across the matrix or membrane of nanochannels. While in the development of the nanoporous thermal machine [34], nanoporous solid framework with much higher stiffness might be desirable to keep a constant infiltration pressure and thus a stable working performance, even under the condition of mild increment of ambient temperature.

ACKNOWLEDGMENT

The work is supported by NSF under Grants No. CMMI-0643726 (X.C.) and No. CMS-0409521 (P.J.C). L.L acknowledges the support of the Founder's Prize, through the American Academy of Mechanics, sponsored by the Robert M. and Mary Haythornthwaite Foundation. X.C. is also supported by a WCU (World Class University) program through the National Research Foundation of Korea funded by the Ministry of Education, Science and Technology of Korea (R32–2008–000–20042–0). X.C. is also supported by the National Natural Science Foundation of China, Grant No. 50928601.

[1] R. H. Baughman, A. A. Zakhidov, and W. A. d. Heer, Science **297**, 787 (2002).
[2] X. Chen and G. Cao, J. Comput. Theor. Nanosci. **4**, 823 (2007).
[3] J. Cao, Q. Wang, M. Rolandi, and H. Dai, Phys. Rev. Lett. **93**, 216803 (2004).
[4] S. N. Kim, J. F. Rusling, and F. Papadimitrakopoulos, Adv. Mater. **19**, 3214 (2007).
[5] X. Chen and Y. Huang, J. Eng. Mech. **134**, 211 (2008).
[6] L. Liu and X. Chen, J. Phys. Chem. B **113**, 6468 (2009).
[7] A. C. Dillon, K. M. Jones, T. A. Bekkedahl, C. H. Kiang, D. S. Bethune, and M. J. Heben, Nature (London) **386**, 377 (1997).
[8] M. A. Shannon, P. W. Bohn, M. Elimelech, J. G. Georgiadis, and B. J. Mariñas, Nature **452**, 301 (2008).
[9] C. Li, E. T. Thostenson, and T.-W. Chou, Compos. Sci. Technol. **68**, 1227 (2008).
[10] M. Whitby and N. Quirke, Nat. Nanotechnol. **2**, 87 (2007).
[11] J. A. Garate, N. J. English, and J. M. D. MacElroy, Mol. Simul. **35**, 3 (2009).
[12] X. Chen, F. B. Surani, X. Kong, V. K. Punyamurtula, and Y. Qiao, Appl. Phys. Lett. **89**, 241918 (2006).
[13] X. Chen, G. Cao, A. Han, V. K. Punyamurtula, L. Liu, P. J. Culligan, T. Kim, and Y. Qiao, Nano Lett. **8**, 2988 (2008).
[14] L. Liu, Y. Qiao, and X. Chen, Appl. Phys. Lett. **92**, 101927 (2008).
[15] L. Liu, X. Chen, W. Lu, A. Han, and Y. Qiao, Phys. Rev. Lett. **102**, 184501 (2009).
[16] Y. Qiao, L. Liu, and X. Chen, Nano Lett. **9**, 984 (2009).
[17] D. Mattia and Y. Gogotsi, Microfluid. Nanofluid. **5**, 289 (2008).
[18] C.-c. Chiu, G. R. Dieckmann, and S. O. Nielsen, J. Phys. Chem. B **112**, 16326 (2008).
[19] J. Liu, A. G. Rinzler, H. Dai, J. H. Hafner, R. K. Bradley, P. J. Boul, and A. Lu, Science **280**, 1253 (1998).
[20] M. P. Rossi, H. Ye, Y. Gogotsi, S. Babu, P. Ndungu, and J.-C. Bradley, Nano Lett. **4**, 989 (2004).
[21] Y. Gogotsi, N. Naguib, and J. A. Libera, Chem. Phys. Lett. **365**, 354 (2002).
[22] J. H. Walther, R. Jaffe, T. Halicioglu, and P. Koumoutsakos, J. Phys. Chem. B **105**, 9980 (2001).
[23] T. Werder, J. H. Walther, R. L. Jaffe, T. Halicioglu, F. Noca, and P. Koumoutsakos, Nano Lett. **1**, 697 (2001).
[24] L. Liu, J. Zhao, C.-Y. Yin, P. J. Culligan, and X. Chen, Phys. Chem. Chem. Phys. **11**, 6520 (2009).
[25] W. Lu, A. Han, T. Kim, V. K. Punyamurtula, X. Chen, and Y. Qiao, Appl. Phys. Lett. **94**, 023106 (2009).
[26] W. Lu, T. Kim, A. Han, X. Chen, and Y. Qiao, Langmuir **25**, 9463 (2009).
[27] G. Cao, Y. Qiao, Q. Zhou, and X. Chen, Philos. Mag. Lett. **88**, 371 (2008).
[28] G. Cao, Y. Qiao, Q. Zhou, and X. Chen, Mol. Simul. **34**, 1267 (2008).
[29] L. Coiffard and V. Eroshenko, J. Colloid Interface Sci. **300**, 304 (2006).
[30] L. Liu, J. Zhao, P. J. Culligan, Y. Qiao, and X. Chen, Langmuir **25**, 11862 (2009).

[31] N. J. Shirtcliffe, G. McHale, M. I. Newton, C. C. Perry, and P. Roach, Chem. Commun. (Cambridge) **2005**, 3135.
[32] Y. Qiao, V. K. Punyamurtula, A. J. Han, X. G. Kong, and F. B. Surani, Appl. Phys. Lett. **89**, 251905 (2006).
[33] A. Han and Y. Qiao, Philos. Mag. Lett. **87**, 25 (2007).
[34] A. Han and Y. Qiao, Appl. Phys. Lett. **91**, 173123 (2007).
[35] A. Han and Y. Qiao, J. Mater. Res. **22**, 644 (2007).
[36] Y. Qiao, G. Cao, and X. Chen, J. Am. Chem. Soc. **129**, 2355 (2007).
[37] J. A. Thomas and A. J. H. McGaughey, Nano Lett. **8**, 2788 (2008).
[38] Y. Q. Xue and M. D. Chen, Nanotechnology **17**, 5216 (2006).
[39] A. Barreiro, R. Rurali, E. R. Hernández, J. Moser, T. Pichler, L. Forró, and A. Bachtold, Science **320**, 775 (2008).
[40] S. Andreev, D. Reichman, and G. HummerJ. Chem. Phys. **123**, 194502 (2005).
[41] C. V. Nguyen, L. Delzeit, A. M. Cassell, J. Li, J. Han, and M. Meyyapan, Nano Lett. **2**, 1079 (2002).
[42] A. Wongkoblap, D. D. Do, and Y. Wang, J. Colloid Interface Sci. **331**, 65 (2009).
[43] V. K. Punyamurtula and Y. Qiao, Mater. Res. Innovations **11**, 37 (2007).
[44] M. J. Longhurst and N. Quirkea, J. Phys. Chem. B **125**, 184705 (2006).
[45] X. Gong, J. Li, H. Zhang, R. Wan, H. Lu, S. Wang, and H. Fang, Phys. Rev. Lett. **101**, 257801 (2008).
[46] http://lammps.sandia.gov
[47] S. J. Plimpton, J. Comput. Phys. **117**, 1 (1995).
[48] H. A. Zambrano, J. H. Walther, P. Koumoutsakos, and I. F. Sbalzarini, Nano Lett. **9**, 66 (2009).
[49] H. J. C. Berendsen, J. R. Grigera, and T. P. Straatsma, J. Phys. Chem. **91**, 6269 (1987).
[50] R. Hockney and J. Eastwood, *Computer Simulation Using Particles* (Taylor & Francis Inc., Bristol, PA, 1981).
[51] R. S. Taylor, L. X. Dang, and B. C. Garrett, J. Phys. Chem. **100**, 11720 (1996).
[52] S. H. Lee and J. C. Rasaiah, J. Phys. Chem. **100**, 1420 (1996).
[53] H. M. Lu and Q. Jiang, Langmuir **21**, 779 (2005).
[54] R. Qiao and N. R. Aluru, Colloids Surf., A **267**, 103 (2005).
[55] W. L. Jorgensen and J. D. Madura, Mol. Phys. **56**, 1381 (1985).
[56] G. A. Jeffrey, *An Introduction to Hydrogen Bonding (Topics in Physical Chemistry)* (Oxford University Press, New York, 1997).
[57] C. J. Fecko, J. D. Eaves, J. J. Loparo, A. Tokmakoff, and P. L. Geissler, Science **301**, 1698 (2003).
[58] F. B. Surani, X. Kong, and Y. Qiao, Appl. Phys. Lett. **87**, 163111 (2005).
[59] J. Zhao, Y. Qiao, P. J. Culligan, and X. Chen, J. Comput. Theor. Nanosci. (to be published).
[60] V. L. Streeter, E. B. Wylie, and K. W. Bedford, *Fluid Mechanics* (McGraw-Hill Higher Education, New York, 1998).
[61] F. Fornasiero, H. G. Park, J. K. Holt, M. Stadermann, C. P. Grigoropoulos, A. Noy, and O. Bakajin, Proc. Natl. Acad. Sci. U.S.A. **105**, 17250 (2008).